Growth Dynamics of Photoinduced Domains in Two-Dimensional Charge-Ordered Conductors Depending on Stabilization Mechanisms

Yasuhiro Tanaka[1] [*] and Kenji Yonemitsu[1,2] [†]

[1]*Institute for Molecular Science, Okazaki, Aichi 444-8585, Japan*
[2]*Department of Functional Molecular Science, Graduate University for Advanced Studies, Okazaki, Aichi 444-8585, Japan*

Photoinduced melting of horizontal-stripe charge orders in quasi-two-dimensional organic conductors θ-(BEDT-TTF)$_2$RbZn(SCN)$_4$ [BEDT-TTF=bis(ethylenedithio)tetrathiafulvalene] and α-(BEDT-TTF)$_2$I$_3$ is investigated theoretically. By numerically solving the time-dependent Schrödinger equation, we study the photoinduced dynamics in extended Peierls-Hubbard models on anisotropic triangular lattices within the Hartree-Fock approximation. The melting of the charge order needs more energy for θ-(BEDT-TTF)$_2$RbZn(SCN)$_4$ than for α-(BEDT-TTF)$_2$I$_3$, which is a consequence of the larger stabilization energy in θ-(BEDT-TTF)$_2$RbZn(SCN)$_4$. After local photoexcitation in the charge ordered states, the growth of a photoinduced domain shows anisotropy. In θ-(BEDT-TTF)$_2$RbZn(SCN)$_4$, the domain hardly expands to the direction perpendicular to the horizontal-stripes. This is because all the molecules on the hole-rich stripe are rotated in one direction and those on the hole-poor stripe in the other direction. They modulate horizontally connected transfer integrals homogeneously, stabilizing the charge order stripe by stripe. In α-(BEDT-TTF)$_2$I$_3$, lattice distortions locally stabilize the charge order so that it is easily weakened by local photoexcitation. The photoinduced domain indeed expands in the plane. These results are consistent with recent observation by femtosecond reflection spectroscopy.

KEYWORDS: photoinduced phase transition, charge order, metal-insulator transition

1. Introduction

Low-dimensional organic conductors are known to offer a playground for studying strongly correlated electron systems in which various interesting ground states emerge.[1,2] The typical examples are Mott and charge-ordered insulating states, where electron-electron as well as electron-phonon (e-ph) interactions have important roles. In such systems, photoirradiation may induce a phase transition, which has been extensively studied recently[3–6] since it will lead to novel transient phenomena and possible control of various functions of materials.

The quasi-two-dimensional organic conductors θ-(BEDT-TTF)$_2$RbZn(SCN)$_4$ (abbreviated as θ-RbZn hereafter) and α-(BEDT-TTF)$_2$I$_3$ (as α-I$_3$) are typical compounds that exhibit a charge order (CO).[7–10] They consist of stacking layers of monovalent anions and donor BEDT-TTF molecules whose π-band is 3/4-filled. The photoinduced melting of the COs in these systems has recently been observed by using femtosecond reflection spectroscopy.[6,11] It shows a marked difference between their photoinduced dynamics. For α-I$_3$, a semimacroscopic metallic domain is generated, whereas the CO only locally melts for θ-RbZn. In particular, the dynamics in α-I$_3$ shows critical slowing down and strong dependence on the excitation intensity and temperature.[6]

This clear difference is considered to originate from different roles of lattice distortions in stabilizing the COs. In fact, the CO transition in θ-RbZn is a first-order metal-insulator transition with large structural distortion at $T_c = 200$K.[12,13] On the other hand, α-I$_3$ under-

goes small lattice distortion at the CO transition with $T_c = 135$K.[14,15] In both salts, a horizontal-stripe CO is formed, as confirmed by several experiments such as X-ray scattering[13,15] and Raman spectroscopy.[16,17]

Theoretically, CO phenomena have been investigated by using extended Hubbard models including on-site (U) and intersite (V_{ij}) Coulomb interactions.[18–35] The stability of various CO patterns in some members of (BEDT-TTF)$_2$X has been discussed first within the Hartree approximation by considering realistic band structures of (BEDT-TTF)$_2$X.[1,18] The horizontal-stripe CO is shown to be stabilized in θ-RbZn and also in α-I$_3$[18] if the transfer integrals are based on the low-temperature crystal structures with lattice distortions implicitly included. The effects of e-ph interactions on the horizontal COs have been investigated by the Hartree-Fock approximation and exact diagonalization.[30–34] Here the transfer integrals are based on the high-temperature crystal structures if the lattice is undistorted. The results show that charge frustration due to the Coulomb interactions on a triangular lattice and lattice distortion relieving the frustration are essential for θ-RbZn, while the low-symmetry configuration of transfer integrals is important for α-I$_3$. These theoretical studies consistently interpret the experimental findings including the large discontinuity at the CO transition in θ-RbZn and the difference between the behaviors of the spin degrees of freedom in the two salts below T_c.[12,36] Therefore, it is of great importance to investigate the photoinduced melting of the COs and to compare their dynamics.

In this paper, we investigate the photoinduced melting dynamics in θ-RbZn and in α-I$_3$ using the time-dependent Schrödinger equation for extended Hubbard

[*]yasuhiro@ims.ac.jp
[†]kxy@ims.ac.jp

models with Peierls-type e-ph couplings within the Hartree-Fock approximation. It is found that the CO in θ-RbZn is more stable against photoexcitation than that in α-I$_3$, which is consistent with the experimental results.[6] Their dynamics show different behaviors owing to different roles of e-ph couplings for the COs and different underlying crystal structures. In particular, a photoinduced domain with suppressed CO grows anisotropically in θ-RbZn, whereas it grows isotropically in α-I$_3$. This suggests that a macroscopic domain is more easily created in α-I$_3$ than in θ-RbZn. In §2, the extended Peierls-Hubbard model is defined. The numerical method for solving the time-dependent Schrödinger equation is also given. After presenting linear absorption spectra in §3, we show photoinduced dynamics during and after a spatially uniform, oscillating electric field is introduced in §4. The growth of a photoinduced domain after local melting of the CO is discussed in §5. Section 6 is devoted to a summary.

2. Extended Peierls-Hubbard Model on Triangular Lattice

In order to describe the horizontal CO with lattice distortion in θ-RbZn and α-I$_3$, we consider the following extended Peierls-Hubbard model[30–34]

$$H = H_{\mathrm{el}} + H_{\mathrm{lat}} \ , \tag{1}$$

with

$$
\begin{aligned}
H_{\mathrm{el}} &= \sum_{\langle ij \rangle \sigma} \left[(t_{i,j} + \alpha_{i,j} u_{i,j}) e^{i(e/\hbar c)\boldsymbol{\delta}_{i,j} \cdot \boldsymbol{A}(t)} c_{i\sigma}^{\dagger} c_{j\sigma} + \mathrm{H.c.} \right] \\
&+ U \sum_i n_{i\uparrow} n_{i\downarrow} + \sum_{\langle ij \rangle} V_{i,j} n_i n_j \ ,
\end{aligned}
\tag{2}
$$

$$H_{\mathrm{lat}} = \sum_{\langle ij \rangle} \frac{K_{i,j}}{2} u_{i,j}^2 + \sum_{\langle ij \rangle} \frac{K_{i,j}}{2\omega_{i,j}^2} \dot{u}_{i,j}^2 \ , \tag{3}$$

where $\langle ij \rangle$ represents the summation over pairs of neighboring sites, $c_{i\sigma}^{\dagger}$ ($c_{i\sigma}$) denotes the creation (annihilation) operator for an electron with spin σ at the ith site, $n_{i\sigma} = c_{i\sigma}^{\dagger} c_{i\sigma}$, and $n_i = n_{i\uparrow} + n_{i\downarrow}$. The electron density is fixed at 3/4 filling. The on-site repulsion is denoted by U. For the intersite Coulomb interactions $V_{i,j}$, we consider nearest-neighbor interactions V_c in the vertical direction and V_p in the diagonal direction, as shown in Fig. 1(a). The e-ph coupling constant, lattice displacement, elastic constant and bare phonon frequency are denoted by $\alpha_{i,j}$, $u_{i,j}$, $K_{i,j}$ and $\omega_{i,j}$, respectively. We introduce new variables by $y_{i,j} = \alpha_{i,j} u_{i,j}$ and $s_{i,j} = \alpha_{i,j}^2/K_{i,j}$. The notations of the transfer integrals $t_{i,j}$, $y_{i,j}$ and $s_{i,j}$ are the same as those in refs. 32 and 33 for both compounds.

The structures of θ-RbZn and α-I$_3$ in the high- and low-temperature phases are schematically shown in Fig. 1. In the metallic phase of θ-RbZn, there are two kinds of transfer integrals t_p and t_c for the diagonal and vertical bonds, respectively, while the CO transition doubles the unit cell in the c-direction and six transfer integrals appear at low temperatures. On the other hand, the unit cell of α-I$_3$ contains four molecules in both phases. According to the X-ray structural analysis,[15] sites A and A$'$ are equivalent in the metallic phase owing to inver-

sion symmetry, while the symmetry breaks below the CO transition temperature.

In the previous studies,[30, 32, 33] we consider three types of e-ph couplings s_c, s_{p1}, and s_ϕ for θ-RbZn, and two types of e-ph couplings s_{b1} and s_{b2} for α-I$_3$ in order to investigate the roles of all the lattice distortions on the stability of the COs. For θ-RbZn, the high-temperature structure has high symmetry, where several patterns of COs are nearly degenerate because of the charge frustration. The lattice distortions relieve the frustration. We found that s_ϕ, which comes from molecular rotation,[30, 31] is the most important for realizing the horizontal CO. As shown in Fig. 1(c), this distortion homogeneously modulates the horizontally connected transfer integrals,[30, 31] $t_{p2} = t_p - y_\phi$ and $t_{p4} = t_p + y_\phi$, by which the CO is globally stabilized. For α-I$_3$, on the other hand, lattice effects are relatively small and the low-symmetry configuration of transfer integrals stabilizes the horizontal CO,[32, 34] as explained below. Charge disproportionation between sites B and C exists even in the metallic phase[38–41] because the large and nonequivalent transfer integrals t_{b1} and t_{b2} form a zigzag chain,[15] as seen in Fig. 1(b). Since t_{b2} is larger than t_{b1} in the chain, site B (C) becomes hole-rich (hole-poor) so as to gain the kinetic energy. The appearance of the horizontal CO breaks the equivalence of sites A and A$'$. The e-ph couplings s_{b1} and s_{b2} stabilize this CO. However, the configuration of large transfer integrals is not along the hole-rich stripes in contrast to the case of θ-RbZn. In other words, the CO is locally stabilized in α-I$_3$: the distortion causing $t_{B2'} > t_{B2}$ ($t_{B1'} > t_{B1}$) in Fig. 1(d) locally strengthens the bond B2$'$ (B1$'$), which is regarded as the formation of a local singlet on the bond B2$'$. As a consequence, site A (A$'$) becomes hole-rich (hole-poor). With these facts in mind, in the present paper we consider only s_ϕ and s_{b2} as the e-ph coupling in θ-RbZn and α-I$_3$, for simplicity. Because only one phonon mode is taken into account, we set the bare phonon frequency at $\omega_{i,j} = \omega_{\mathrm{ph}}$.

The photoexcitation is introduced by the Peierls phase factors of the transfer integrals in eq. (2). Here $\boldsymbol{\delta}_{i,j}$ denotes the position vector from the ith site to the jth site. The vector potential $\boldsymbol{A}(t)$ is given by,

$$\boldsymbol{A}(t) = -c \int_0^t dt' \boldsymbol{E}(t') \ , \tag{4}$$

$$\boldsymbol{E}(t) = \boldsymbol{E}_{\mathrm{ext}} \theta(t) \theta(T_{\mathrm{irr}} - t) \sin \omega_{\mathrm{ext}} t \ , \tag{5}$$

where $\boldsymbol{E}_{\mathrm{ext}}$ and ω_{ext} is the amplitude and frequency, respectively, of the time-dependent electric field $\boldsymbol{E}(t)$. In eq. (5), we define the pulse width $T_{\mathrm{irr}} = 2\pi N_{\mathrm{ext}}/\omega_{\mathrm{ext}}$ with N_{ext} being an integer. $\theta(t)$ is the Heaviside step function, $\theta(t) = 1$ for $t > 0$ and $\theta(t) = 0$ for $t < 0$. We use $e = 1$, $\hbar = 1$, and the intermolecular distance along the c-axis of θ-RbZn and that along the a-axis of α-I$_3$ as the unit of length. Furthermore, the intermolecular distance along the a-axis of θ-RbZn and that along the b-axis of α-I$_3$ are set at twice the unit length. By these definitions, parameters are given in units of eV unless otherwise noted.
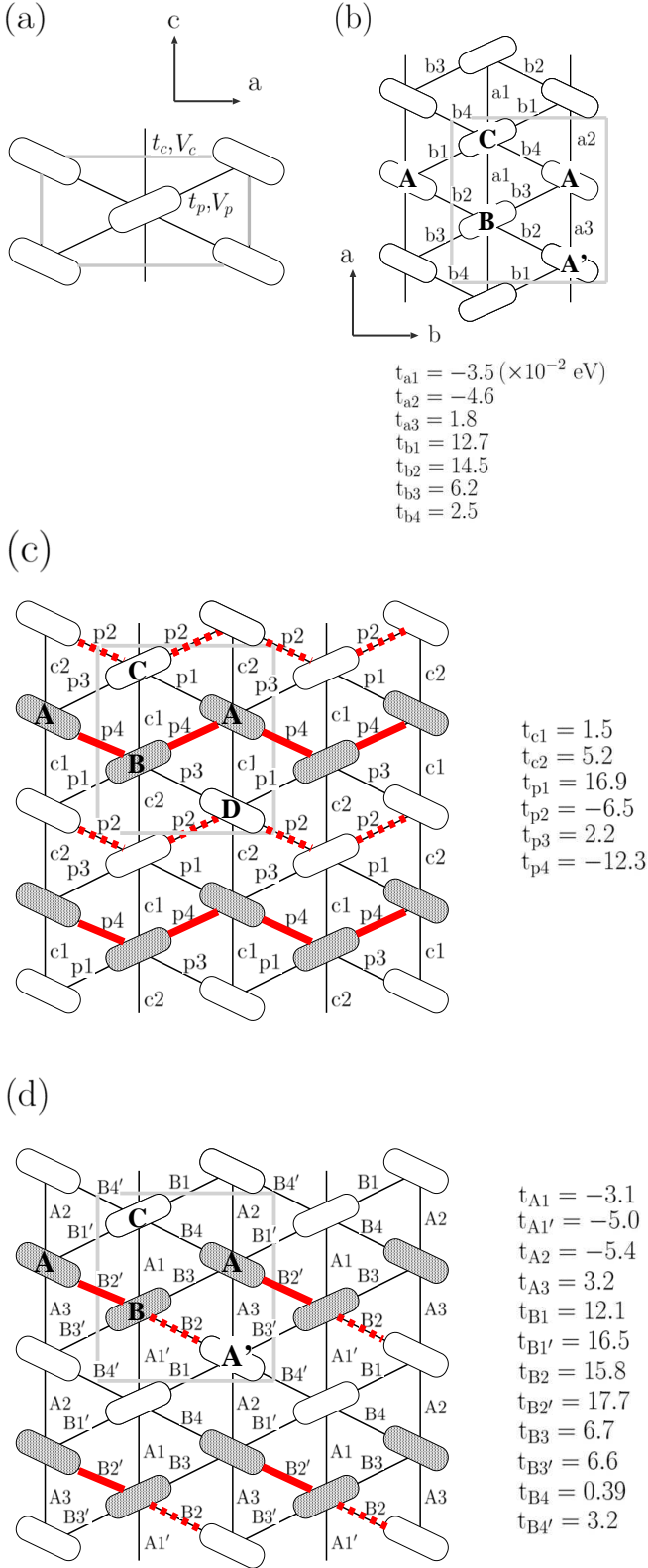
The time evolution of the system is calculated as fol-

(a)

(b)

$t_{a1} = -3.5 \, (\times 10^{-2} \text{ eV})$
$t_{a2} = -4.6$
$t_{a3} = 1.8$
$t_{b1} = 12.7$
$t_{b2} = 14.5$
$t_{b3} = 6.2$
$t_{b4} = 2.5$

(c)

$t_{c1} = 1.5$
$t_{c2} = 5.2$
$t_{p1} = 16.9$
$t_{p2} = -6.5$
$t_{p3} = 2.2$
$t_{p4} = -12.3$

(d)

$t_{A1} = -3.1$
$t_{A1'} = -5.0$
$t_{A2} = -5.4$
$t_{A3} = 3.2$
$t_{B1} = 12.1$
$t_{B1'} = 16.5$
$t_{B2} = 15.8$
$t_{B2'} = 17.7$
$t_{B3} = 6.7$
$t_{B3'} = 6.6$
$t_{B4} = 0.39$
$t_{B4'} = 3.2$

Fig. 1.   (Color online) Schematic representations of the structures of (a) θ-(BEDT-TTF)$_2$X in the metallic phase, (b) α-I$_3$ in the metallic phase,[37] (c) θ-RbZn in the CO phase, and (d) α-I$_3$ in the CO phase. The gray solid lines indicate unit cells. For (b), (c), and (d), the transfer integrals estimated by the extended Hückel method[13, 15] are also shown. The red or thick solid (dashed) lines in (c) and (d) indicate the bonds on which the magnitudes of the transfer integrals are increased (decreased) by the distortions considered in the present paper.

lows. For the electronic part, we use the time-dependent Schrödinger equation,

$$|\psi_{\nu,\sigma}(t + \Delta t)\rangle = T\exp\Big[-i\int_t^{t+\Delta t} dt' H_{\text{el}}^{\text{HF}}(t')\Big]|\psi_{\nu,\sigma}(t)\rangle, \tag{6}$$

where T denotes the time-ordering operator, $|\psi_{\nu,\sigma}(t)\rangle$ the ν-th one-particle state with spin σ at time t, and $H_{\text{el}}^{\text{HF}}$ the electronic part H_{el} in the Hartree-Fock approximation.

For the lattice part, we solve the classical equation of motion by the leapfrog method.[42] In the case of θ-RbZn, we assume that for the lth unit cell the transfer integrals on the two $p4$-bonds connected to site B and those on the two $p2$-bonds connected to site C are given by $t_{p4}(l) = t_p + y_\phi(l)$ and $t_{p2}(l) = t_p - y_\phi(l)$, respectively. The equation of motion for $u_\phi(l)$ is then written as,

$$m_\phi \frac{d^2 u_\phi(l)}{dt^2} = \frac{1}{4} F_l^\theta(t), \tag{7}$$

where we write the force for θ-RbZn as,

$$F_l^\theta(t) = -\Big(\frac{\partial H_{\text{lat}}}{\partial u_\phi(l)} + \langle \Psi(t)|\frac{\partial H_{\text{el}}^{\text{HF}}}{\partial u_\phi(l)}|\Psi(t)\rangle\Big). \tag{8}$$

Here $m_\phi = K_\phi/\omega_{\text{ph}}^2$ is the phonon mass, and $|\Psi(t)\rangle$ is the Slater-determinant composed of the one-particle states $|\psi_{\nu,\sigma}(t)\rangle$. In the case of α-I$_3$, we set $t_{B2'}(l) = t_{b2} + y_{b2}(l)$ and $t_{B2}(l) = t_{b2} - y_{b2}(l)$. The equation of motion for $u_{b2}(l)$ thus reads,

$$m_{b2} \frac{d^2 u_{b2}(l)}{dt^2} = \frac{1}{2} F_l^\alpha(t), \tag{9}$$

where $m_{b2} = K_{b2}/\omega_{\text{ph}}^2$ and $F_l^\alpha(t)$ is defined as in eq. (8). We note that for both compounds the initial state is the horizontal CO state where the lattice displacements do not depend on l.[30–34] When the uniform time-dependent electric field is applied, their response is still uniform. However, they become nonuniform when the electric field is applied locally as in §5.

In the actual calculations, we first obtain $F_l^\theta(t)$ or $F_l^\alpha(t)$ by using the wave function $|\psi_{\nu,\sigma}(t)\rangle$. Then, y_ϕ or y_{b2} at $t + \Delta t$ is calculated, which is accurate to the order of $(\Delta t)^2$. The wave function $|\psi_{\nu,\sigma}(t + \Delta t)\rangle$ is obtained from eq. (6) by,

$$|\psi_{\nu,\sigma}(t+\Delta t)\rangle \simeq \exp\Big[-i\Delta t H_{\text{el}}^{\text{HF}}(t+\tfrac{1}{2}\Delta t)\Big]|\psi_{\nu,\sigma}(t)\rangle, \tag{10}$$

whose error is of the order of $(\Delta t)^3$. In the above equation, we use $H_{\text{el}}^{\text{HF}}(t + \frac{1}{2}\Delta t) = [H_{\text{el}}^{\text{HF}}(t) + H_{\text{el}}^{\text{HF}}(t + \Delta t)]/2$ where $H_{\text{el}}^{\text{HF}}(t + \Delta t)$ is constructed so that it is accurate to the first order of Δt. The exponential operator is expanded with time slice $\Delta t = 0.01$ until the norm of the wave function becomes unity with sufficient accuracy. The obtained $|\psi_{\nu,\sigma}(t + \Delta t)\rangle$ has an error of the order of $(\Delta t)^3$.

In this paper, the phonon frequency $\omega_{\text{ph}} = 0.01$ is used for both compounds. We set $t_p = 0.1$ and $t_c = -0.04$ for θ-RbZn. For the transfer integrals in α-I$_3$, we use the values shown in Fig. 1(b). The system size is fixed at 12×12 sites and the periodic boundary condition is imposed. The interaction strengths and the e-ph coupling constants are chosen at $U = 0.7$, $V_c = 0.4U$, $V_p/V_c = 0.6$,
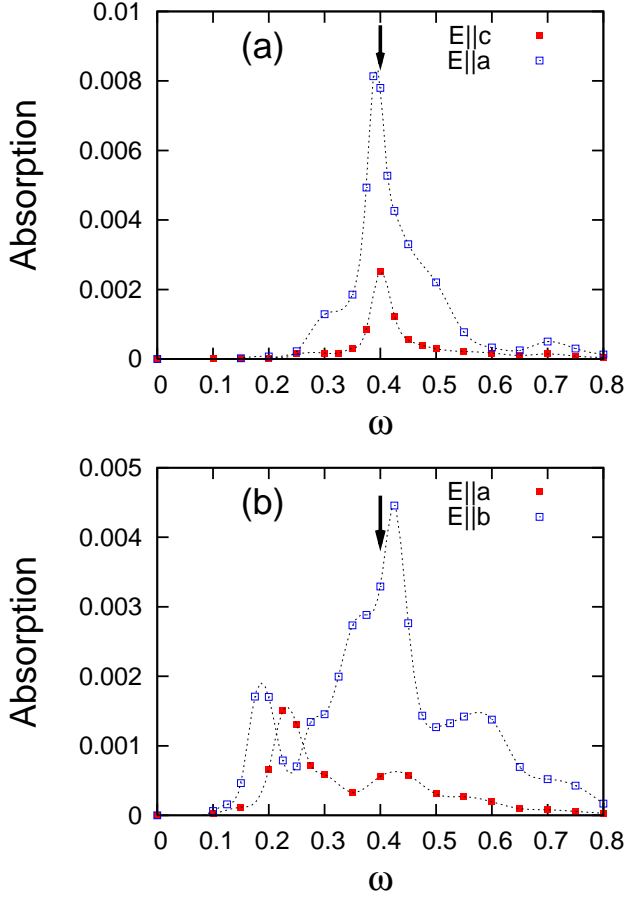
Fig. 2. (Color online) Linear absorption spectra obtained by the time-dependent Hartree-Fock approximation for 12×12-site system with $U=0.7$, $V_c/U=0.4$, and $V_p/V_c=0.6$ for (a) θ-RbZn ($s_\phi=0.1$) and (b) α-I$_3$ ($s_{b2}=0.07$) with different polarizations as indicated. The peak-broadening parameter γ is set at 0.02.

$s_\phi = 0.1$, and $s_{b2} = 0.07$ throughout the study. These parameters give the horizontal CO ground states for both compounds.[30, 32]

3. Linear Absorption Spectra

First, we discuss linear absorption spectra, which correspond to optical conductivity spectra. For this purpose, we replace the electric field in eq. (5) by the one with a damping factor,

$$\boldsymbol{E}(t) = \boldsymbol{E}_{\text{ext}}\theta(t)\exp(-\gamma t)\sin\omega_{\text{ext}}t \ , \qquad (11)$$

and calculate the increment in the total energy due to $\boldsymbol{E}(t)$ with small $\mid \boldsymbol{E}_{\text{ext}} \mid$ at sufficiently large t so that the total energy converges. We use $\mid \boldsymbol{E}_{\text{ext}} \mid = 0.002$ and $\gamma=0.02$ to obtain results shown in Fig. 2. In both cases of θ-RbZn and α-I$_3$, the absorption is larger for the polarization parallel to the stripes, i.e., along the a- and b-axes, respectively, than for the polarization perpendicular to them, i.e., along the c- and a-axes, respectively. This is because the transfer integrals on the diagonal bonds are larger than those on the vertical bonds. The absorption spectra with polarization parallel to the stripes have similar structures with resonance peaks located at around $\omega = 0.4$ for both compounds. Therefore, in the following we show results obtained by the electric field with
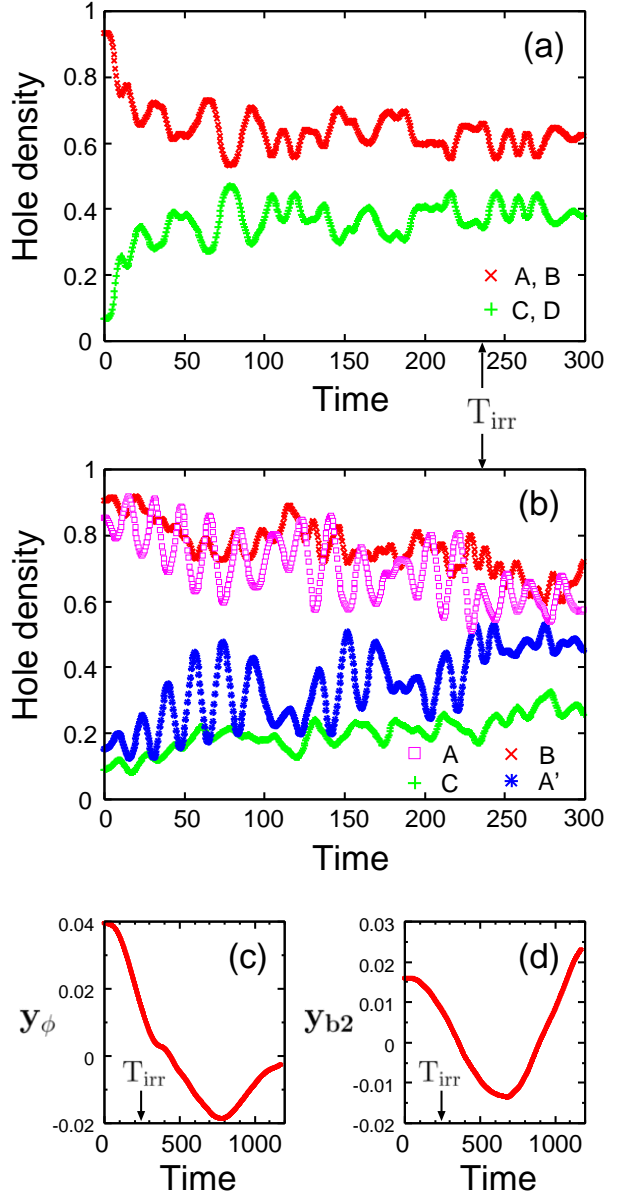

Fig. 3. (Color online) Time dependence of hole densities during ($t < T_{\text{irr}}$) and after ($t > T_{\text{irr}}$) photoexcitation along the stripes for (a) θ-RbZn ($\omega_{\text{ext}}=0.4$, $\mid \boldsymbol{E}_{\text{ext}} \mid = 0.25$) and (b) α-I$_3$ ($\omega_{\text{ext}}=0.4$, $\mid \boldsymbol{E}_{\text{ext}} \mid = 0.04$). The time dependence of modulations in transfer integrals is also shown in (c) and (d), respectively, on a longer timescale.

$\omega_{\text{ext}} = 0.4$ and polarization parallel to the stripes.

4. Photoinduced Melting Dynamics

Next, we discuss photoinduced melting dynamics. Figure 3 shows the time evolution of the hole densities $2 - \langle n_i \rangle$ and the lattice distortions during and after the photoexcitation with $N_{\text{ext}} = 15$ ($T_{\text{irr}} = 236$ corresponding to 155 fs) which is comparable to the experimental pulse width.[6] The unit of time is $(\text{eV})^{-1}$, so that $t = 1520$ corresponds to 1 ps. For both salts, the COs are weakened by photoexcitation, as seen in Figs. 3(a) and 3(b). The amplitude of the electric field is chosen at $\mid \boldsymbol{E}_{\text{ext}} \mid = 0.25$ for θ-RbZn and $\mid \boldsymbol{E}_{\text{ext}} \mid = 0.04$ for α-I$_3$, which is near the critical value for melting the CO. The increment in the total energy per site ΔE is 0.098 and 0.042, respectively.

For θ-RbZn, there are two distinct hole densities at $t = 0$ since each stripe consists of sites with equal hole densities. This is also true at $t > 0$ if the polarization of $\boldsymbol{E}(t)$ is parallel to the stripes as in Fig. 3(a), whereas the hole densities on the four sites in the unit cell become different when the polarization is perpendicular to the stripes. For α-I$_3$, on the other hand, the four sites are already distinct at $t = 0$ because of the low symmetry of the crystal structure.

As for the time dependence of the hole densities, resonantly excited dynamics is clearly seen for α-I$_3$ especially in the oscillation of the hole densities on sites A and A$'$, the periods of which are nearly equal to that of the electric field $2\pi/\omega_{\mathrm{ext}}$ being 15.7. For θ-RbZn, the charge dynamics is more complex than that for α-I$_3$ although ω_{ext} is near the resonance peak of the linear absorption spectrum. Such a difference is also visible in results obtained by the exact many-electron wave functions on small clusters of 12 sites,[43] where the origin of the different behaviors is interpreted with the distribution of energy levels above the ground state, which is denser in θ-RbZn than in α-I$_3$. This is because the high symmetry of the undistorted structure in θ-RbZn causes charge frustration. Therefore, a larger number of excited states are nearly degenerate and involved in the photoinduced dynamics in θ-RbZn, which results in complex charge dynamics.

The time dependence of the lattice distortions y_ϕ and y_{b2} is shown in Figs. 3(c) and 3(d), respectively. Since the COs are almost completely destroyed in the present parameters, the displacements become zero at some t although they oscillate with periods longer than $2\pi/\omega_{\mathrm{ph}}$ by phonon softening, which are much longer than the timescales of charge-transfer excitations. For $\omega_{\mathrm{ph}} = 0.01$, the oscillation period is about 1 ps for both compounds, which is comparable to the experimentally observed value of 0.7 ps (48 cm^{-1}) in the time evolutions of reflectivity spectra.[6]

In order to compare the efficiency of photoinduced melting for θ-RbZn and that for α-I$_3$, we show time-averaged hole densities as a function of ΔE in Figs. 4(a) and 4(b). Here the averages are taken after $t = T_{\mathrm{irr}}$ over the period of $T_{\mathrm{irr}} = 2\pi N_{\mathrm{ext}}/\omega_{\mathrm{ext}} < t < 10\pi N_{\mathrm{ext}}/\omega_{\mathrm{ext}}$. There is a critical value ΔE_c above which the horizontal CO disappears. The value for θ-RbZn, $\Delta E_c = 0.098$, is larger than that for α-I$_3$, $\Delta E_c = 0.042$. This is a consequence of the larger lattice stabilization energy for the horizontal CO in θ-RbZn than that in α-I$_3$.[30–34] We notice that this inequality generally holds for any excitation frequency and for any polarization (not shown). The robustness of the CO in θ-RbZn compared to that in α-I$_3$ against the photoirradiation has been observed in the femtosecond spectroscopy.[6] The efficiency of the photoinduced metallic state by $\omega_{\mathrm{ext}} = 0.89$ eV is evaluated as 100 (θ-RbZn) and 250 (α-I$_3$) molecules/photon. The values of ΔE_c in our calculations are, however, one order of magnitude larger than the experimentally estimated ones. This may be due to the Hartree-Fock approximation, since ΔE_c becomes smaller in our recent study based on the exact many-electron wave functions.[43] Effects of thermal fluctuations and the experimental estimation itself,
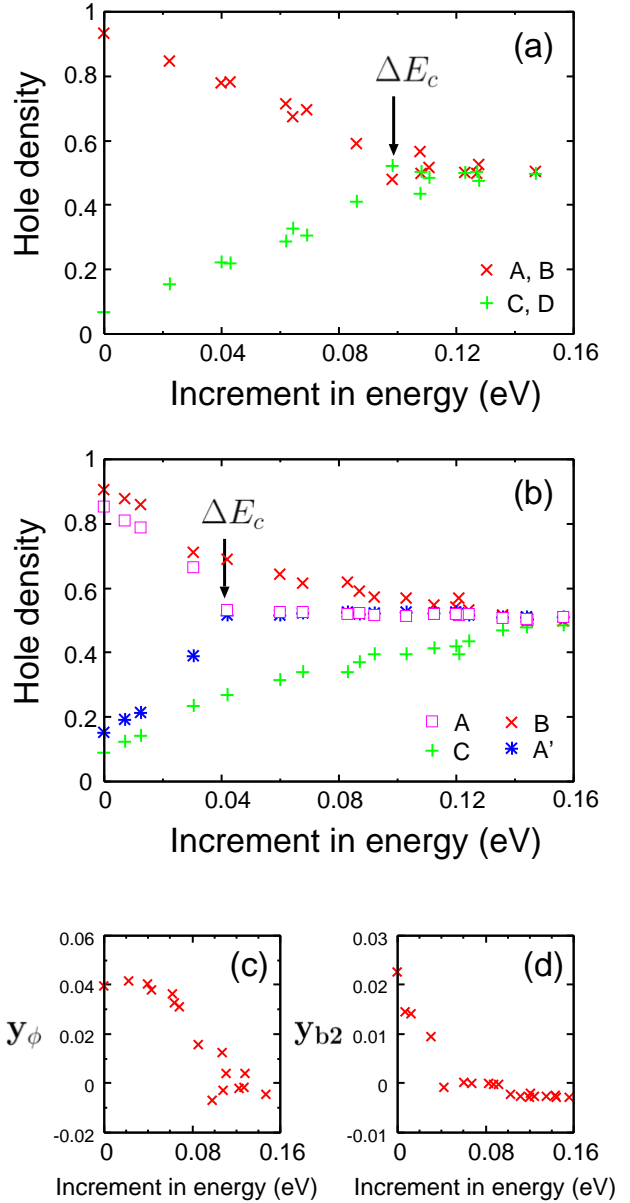

Fig. 4. (Color online) Time-averages of hole densities after photoexcitation along the stripes for (a) θ-RbZn (ω_{ext}=0.4) and (b) α-I$_3$ (ω_{ext}=0.4), as a function of increment in total energy per site ΔE. The time-averages of modulations in transfer integrals y_ϕ and y_{b2} are shown in (c) and (d), respectively.

which generally contains an error depending on the estimation of the penetration depth, are also possible reasons for the discrepancy.

For θ-RbZn, the time-averaged hole distribution becomes uniform above ΔE_c. For α-I$_3$, on the other hand, the averaged hole densities on sites A and A$'$ become equal above ΔE_c while the charge disproportionation on sites B and C remains for larger values of ΔE. This is reminiscent of the fact that the charge disproportionation exists even in the high-temperature metallic phase of α-I$_3$ because of low-symmetry configuration of transfer integrals.[38–41] If we increase ΔE further, the hole densities on the four sites finally merge into 0.5.

In Figs. 4(c) and 4(d), we show the averaged lattice displacements which indicate that both y_ϕ and y_{b2} van-

ish at around ΔE_c. This is reasonable because the y_ϕ distortion is essential for stabilizing the horizontal CO in θ-RbZn, while the y_{b2} distortion breaks the inversion symmetry that guarantees the equivalence of hole densities on sites A and A$'$ in α-I$_3$.

5. Domain Growth after Local Photoexcitation

Recall that the mechanisms for stabilizing the COs by lattice distortions are different in the two salts. In θ-RbZn, the whole hole-rich (hole-poor) stripe is stabilized by strengthening (weakening) the horizontally connected p4 (p2) bonds. In α-I$_3$, the metallic phase without lattice distortion already possesses a hole-rich site B and a hole-poor site C by the relation $t_{b2} > t_{b1}$. The hole-rich site A and the hole-poor site A$'$ bridged by the site B are locally stabilized by strengthening the bond B2$'$ and weakening the bond B2. Thus, local photoexcitations would easily weaken the CO in α-I$_3$, but the CO in θ-RbZn would be robust.

Then, we investigate the growth of photoinduced domains with weakened CO after local photoexcitation, by modifying the model in eq. (2) through the introduction of the Peierls phase factors only on the bonds that connect four sites within a unit cell of the 12×12-site system. The phase factor is set at unity on all the other bonds. The time evolution is calculated by the method explained in §2. In Fig. 5, we show snapshots of the hole densities at $t = 200$, 400 and 600, from which those at $t = 0$ are subtracted, $\langle \Psi(t) | n_i | \Psi(t) \rangle - \langle \Psi(0) | n_i | \Psi(0) \rangle$, during and after the local photoexcitation with $\omega_{ext} = 0.4$ and $N_{ext} = 15$ ($T_{irr} = 236$). The polarization is parallel to the stripes. In the figures, the bonds on which the photoexcitation is applied are located at (7.5,7), (7.5,7.5), and (7.5,8). Here, the location of the bond between the sites at (i_x, i_y) and (j_x, j_y) is denoted by $(\frac{i_x+j_x}{2}, \frac{i_y+j_y}{2})$. For θ-RbZn (α-I$_3$), these bonds correspond to B-D (B-A$'$), B-A, and C-A or p3 (B2), p4 (b3), and p1 (b4) respectively, in Fig. 1. In order to compare the growth dynamics, we set $| \boldsymbol{E}_{ext} | = 0.6$ for θ-RbZn and $| \boldsymbol{E}_{ext} | = 0.32$ for α-I$_3$, which lead to the ratio $\Delta E / \Delta E_c \sim 0.4$ for both compounds. Here ΔE_c is the value obtained in §4 by the uniform photoexcitation, whereas ΔE is the increment in the total energy per site after the local photoexcitation.

In Fig. 5, the growth of the domain shows anisotropy, which is pronounced in θ-RbZn. Namely, the growth of the domain is faster to the direction parallel to the stripes than to that perpendicular to the stripes for both compounds. This is caused by the anisotropy in the transfer integrals which are larger for the p- and b-bonds than for the c- and a-bonds in θ-RbZn and α-I$_3$, respectively. For θ-RbZn, the hole densities largely deviate from those at $t = 0$ only on the horizontal rows near the four photoexcited sites. The amount of change reaching 0.5 means that the CO is completely destroyed in this region. In the vertical direction, however, the growth is strongly suppressed. For α-I$_3$, the photoinduced domain expands over the whole system at $t = 600$ although the largest amount of change in the hole densities is smaller than that in θ-RbZn.

In order to analyze the domain growth more quantitatively, we show $\Delta E / \Delta E_c$ as a function of $| \boldsymbol{E}_{ext} |^2$ in Fig.
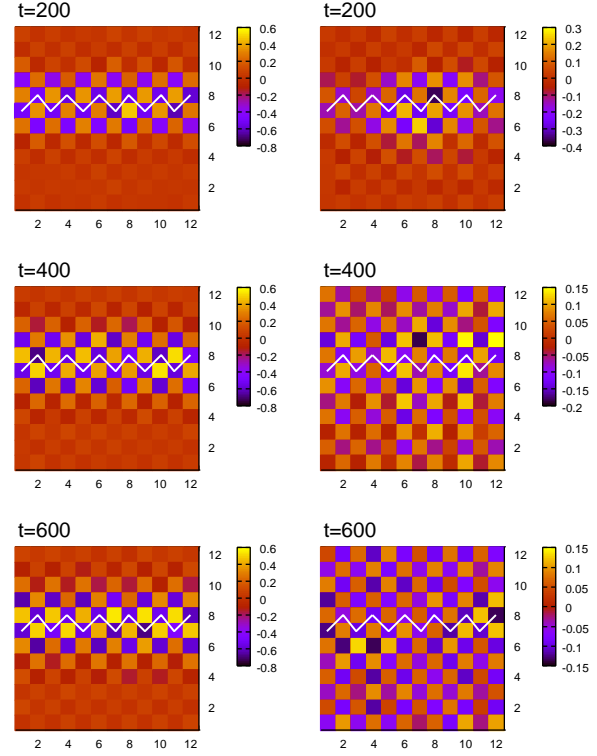

Fig. 5. (Color online) Hole densities at $t = 200, 400$ and 600 from top to bottom, from which those at $t = 0$ are subtracted, for $\omega_{ext} = 0.4$ and $N_{ext} = 15$. The left and right panels show θ-RbZn for $| \boldsymbol{E}_{ext} | = 0.6$ and α-I$_3$ for $| \boldsymbol{E}_{ext} | = 0.32$, respectively, where the squares indicate sites and the white lines indicate hole-rich stripes. The photoexcitation with polarization parallel to the stripes is introduced only on the bonds (7.5,7), (7.5,7.5), and (7.5,8), which correspond to B-D (B-A$'$), B-A, and C-A or p3 (B2), p4 (b3), and p1 (b4) for θ-RbZn (α-I$_3$), respectively.
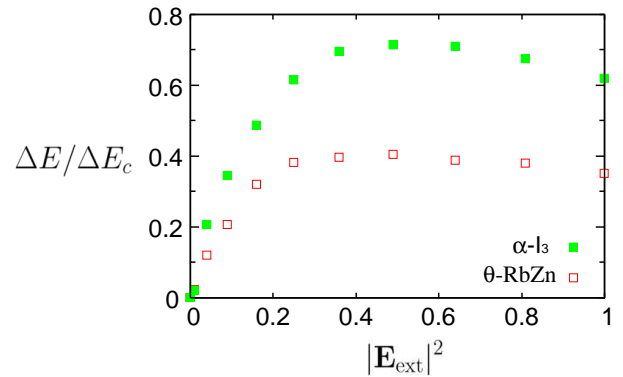

Fig. 6. (Color online) $\Delta E / \Delta E_c$ as a function of $| \boldsymbol{E}_{ext} |^2$ for θ-RbZn and α-I$_3$ after local photoexcitation with polarization parallel to the stripes, $\omega_{ext} = 0.4$, and $N_{ext} = 15$.

6. For both compounds, $\Delta E / \Delta E_c$ has a maximum value as explained in Appendix, which is below unity. Thus, the CO is not globally destroyed by the local photoexcitation with small pulse width. The maximum value is larger for α-I$_3$ than for θ-RbZn, which means that it is more difficult to weaken the CO in θ-RbZn by the local photoexcitation with this pulse width.

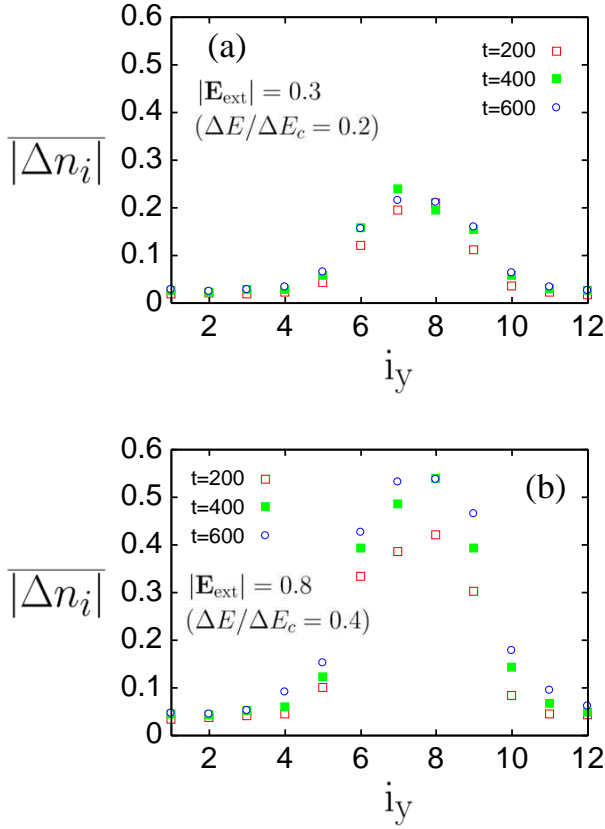The absolute values of the differences between the hole densities at $t = 0$ and those at $t = 200$, 400 and 600 are

Fig. 7. (Color online) The i_y-dependence of $\overline{|\Delta n_i|}$ at $t = 200$, 400, and 600 for (a) $|\boldsymbol{E}_{\mathrm{ext}}| = 0.3$ and (b) $|\boldsymbol{E}_{\mathrm{ext}}| = 0.8$ in the case of θ-RbZn, where i_y is the coordinate along the c-axis. The photoexcitation is along the stripes, $\omega_{\mathrm{ext}} = 0.4$, and $N_{\mathrm{ext}} = 15$.

Fig. 8. (Color online) The i_y-dependence of $\overline{|\Delta n_i|}$ at $t = 200$, 400, and 600 for (a) $|\boldsymbol{E}_{\mathrm{ext}}| = 0.4$ and (b) $|\boldsymbol{E}_{\mathrm{ext}}| = 0.8$ in the case of α-I$_3$, where i_y is the coordinate along the a-axis. The photoexcitation is along the stripes, $\omega_{\mathrm{ext}} = 0.4$, and $N_{\mathrm{ext}} = 15$.

averaged over the direction parallel to the stripes and denoted by $\overline{|\Delta n_i|}$:

$$\overline{|\Delta n_i|} = \frac{1}{L_x} \sum_{i_x} |\langle \Psi(t)|n_i|\Psi(t)\rangle - \langle \Psi(0)|n_i|\Psi(0)\rangle|, \quad (12)$$

where $L_x = 12$ is the number of sites along the a- and b-axes for θ-RbZn and α-I$_3$, respectively. Thus, we can measure the growth of the photoinduced domain to the direction perpendicular to the stripes. The values $\overline{|\Delta n_i|}$ are plotted as a function of i_y in Fig. 7 for θ-RbZn and in Fig. 8 for α-I$_3$, where i_y is the coordinate along the c- and a-axes (which are perpendicular to the stripes) for θ-RbZn and α-I$_3$, respectively, as used in Fig. 5. Although the charge order on the stripes containing the photoexcited bonds (7.5,7), (7.5,7.5), and (7.5,8) is weakened and the quantities $\overline{|\Delta n_i|}$ at $i_y = 7$ and 8 are increased by increasing $|\boldsymbol{E}_{\mathrm{ext}}|$ from 0.3 to 0.8 for θ-RbZn, the photoinduced domain remains localized near $i_y = 7$ and 8. In other words, the photoinduced domain hardly grows to the direction perpendicular to the stripes. The influence of the local photoexcitation is confined in a region near the photoexcited bonds. This property prevents $\Delta E/\Delta E_c$ from becoming large beyond the maximum value, as shown in Fig. 6. For α-I$_3$, the domain growth is qualitatively different from that in θ-RbZn. The photoinduced domain expands to the vertical direction as shown in Fig. 8(a) for $|\boldsymbol{E}_{\mathrm{ext}}| = 0.4$, although the
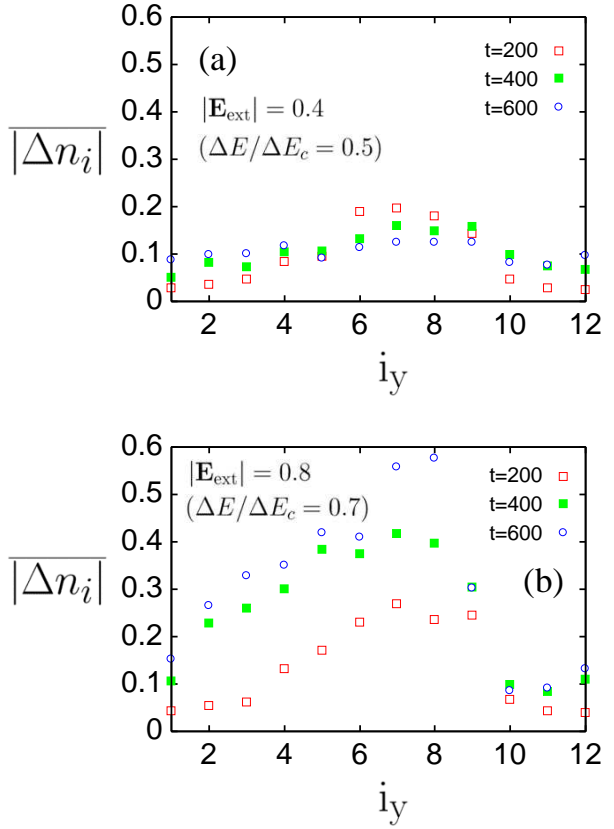
values of $\overline{|\Delta n_i|}$ are relatively small. When we increase $|\boldsymbol{E}_{\mathrm{ext}}|$, a large region of suppressed CO (i.e., large $\overline{|\Delta n_i|}$) is created as shown in Fig. 8(b). It is noted that the i_y-dependence of $\overline{|\Delta n_i|}$ is asymmetric for α-I$_3$. The photoinduced domain expands to the direction of decreasing i_y more easily than to the direction of increasing i_y. This feature is generally observed irrespective of the choice of photoexcited bonds because it reflects the asymmetry of the charge distribution that allows the ferroelectricity.[44] Let us focus a region near the bond B2$'$ connecting sites A and B that has the largest transfer integral $t_{\mathrm{B2}'}$ (see Fig. 1). The transfer integrals t_{b1} and t_{b4} connecting sites A and C are different from t_{B2} and t_{b3} connecting sites B and A$'$. When the local distortion at site B making $t_{\mathrm{B2}'} > t_{B2}$ is weakened by photoexcitation, the hole is locally transferred from site A through site B to site A$'$. This corresponds to the direction that weakens the ferroelectric polarization. This results in the asymmetry of $\overline{|\Delta n_i|}$. It is in contrast to $\overline{|\Delta n_i|}$ for θ-RbZn, where the transfer integrals t_p connecting sites A and C are the same as t_p connecting sites B and D.

These numerical results suggest that a macroscopic domain is much more easily created in α-I$_3$ than in θ-RbZn. They are consistent with the experimental observations by the time evolutions of reflectivity spectra,[6] which indicate the growth of a metallic domain only for α-I$_3$, although spatial inhomogeneity is not directly observed. The critical slowing down observed in α-I$_3$[6] is beyond the

scope of the present study. If we consider it theoretically, we would need to treat larger system and domain sizes. Effects of relaxation, which are not taken into account here, may also be important for the dynamics on longer timescales.

The different growth dynamics is caused by the different mechanisms of stabilizing the COs: the CO in θ-RbZn is stabilized stripe by stripe through the homogeneous modulation of transfer integrals along the stripes, while the CO in α-I$_3$ is stabilized locally, as explained in §2. The growth dynamics is thus qualitatively unchanged even if we use different excitation frequencies and polarizations in the calculations.

6. Summary

We have investigated the photoinduced melting dynamics of COs in quasi-two-dimensional organic conductors θ-RbZn and α-I$_3$. Although they show COs with similar horizontal-stripe patterns, relative importance of e-ph couplings and their configurations of transfer integrals in stabilizing the COs are quite different.[30–34] By numerically solving the time-dependent Schödinger equation within the Hartree-Fock approximation, charge and lattice dynamics are obtained in the extended Peierls-Hubbard models during and after the oscillating electric field is introduced with and without spatial dependence. We find different photoinduced dynamics in these salts, which originate from different mechanisms of stabilizing the COs by lattice distortions.

In the case of a spatially uniform time-dependent electric field, we calculated time-averaged hole densities as a function of the increment in the total energy per site ΔE. We find a critical value ΔE_c above which the horizontal CO and the lattice distortion simultaneously disappear. The ΔE_c value in θ-RbZn is larger than that in α-I$_3$, as a consequence of the larger stabilization energy for the CO in θ-RbZn. When the COs are destroyed, the hole distribution reflects the symmetry of the underlying crystal structure without lattice distortions. It becomes uniform for θ-RbZn whereas the charge disproportionation between sites B and C remains for α-I$_3$.

When the applied electric field is local, the time evolution of the hole densities shows anisotropy. The influences of the local photoexcitation propagate more rapidly to the direction parallel to the stripes than to that perpendicular to the stripes. In particular, for θ-RbZn a photoinduced domain hardly expands to the perpendicular direction. The increase of $\Delta E/\Delta E_c$ is limited to a small value when the pulse width is small, indicating that it is difficult to melt the CO in θ-RbZn by the local photoexcitation. This is because the y_ϕ-distortion homogeneously modulates the transfer integrals on the horizontally connected bonds, so that the charge correlation in each stripe (between stripes) is strong (weak). For α-I$_3$, on the other hand, the photoinduced domain expands in the plane. This comes from the fact that each hole-rich bond B2$'$ between sites A and B in α-I$_3$ is locally stabilized by the y_{b2}-distortion.

The obtained results are qualitatively consistent with the experimental observations, which indicate that the CO in θ-RbZn is more stable against photoexcitation than in α-I$_3$: a macroscopic metallic domain is generated in α-I$_3$ whereas the CO only locally melts in θ-RbZn.

Appendix: Maximum of Increment in Total Energy

Figure 6 shows that $\Delta E/\Delta E_c$ begins to decrease at around $| \boldsymbol{E}_{\text{ext}} |= 0.7$ ($| \boldsymbol{E}_{\text{ext}} |^2 = 0.5$). This behavior comes as a consequence of the periodicity of the energy band in momentum space. The electric field shifts the momenta of electrons. For simplicity, let us consider the noninteracting electrons in one-dimension, where the shift is estimated by the equation of motion,

$$\frac{dk}{dt} = E_{\text{ext}} \sin \omega_{\text{ext}} t. \qquad (\text{A·1})$$

Here k is the wave number and we set $e = a = \hbar = 1$ with a being the lattice constant. By integrating the above equation from $t = 0$ to $t = \pi/\omega_{\text{ext}}$ that is one half of the period of the oscillating electric field, we obtain the momentum shift $|\Delta k|$ as,

$$|\Delta k| = \frac{2E_{\text{ext}}}{\omega_{\text{ext}}}. \qquad (\text{A·2})$$

As E_{ext} increases, $|\Delta k|$ and ΔE increase. When $|\Delta k| \sim \pi$, however, some electrons accelerated by the electric field cross the boundary of the Brillouin zone so that $|\Delta k|$ is no longer proportional to E_{ext}. If we increase E_{ext} further, it is expected that the total energy is not efficiently increased any more and even decreases because more electrons cross the zone boundary. This results in the decrease of $\Delta E/\Delta E_c$ as shown in Fig. 6. For $\omega_{\text{ext}} = 0.4$, $|\Delta k| \sim \pi$ corresponds to $E_{\text{ext}} \sim 0.6$, which is consistent with the above value, $| \boldsymbol{E}_{\text{ext}} |= 0.7$.

1) H. Seo, C. Hotta, and H. Fukuyama: Chem. Rev. **104** (2004) 5005.
2) H. Seo, J. Merino, H. Yoshioka, and M. Ogata: J. Phys. Soc. Jpn. **75** (2006) 051009.
3) K. Nasu: *Photoinduced Phase Transitions* (World Scientific, New Jersey, 2004).
4) K. Yonemitsu and K. Nasu: Phys. Rep. **465** (2008) 1.
5) H. Okamoto, K. Ikegami, T. Wakabayashi, Y. Ishige, J. Togo, H. Kishida and H. Matsuzaki: Phys. Rev. Lett. **96** (2006) 037405.
6) S. Iwai, K. Yamamoto, A. Kashiwazaki, F. Hiramatsu, H. Nakaya, Y. Kawakami, K. Yakushi, H. Okamoto, H. Mori, and Y. Nishio: Phys. Rev. Lett. **98** (2007) 097402.
7) K. Miyagawa, A. Kawamoto, and K. Kanoda: Phys. Rev. B **62** (2000) R7679.
8) R. Chiba, H. Yamamoto, K. Hiraki, T. Takahashi, and T. Nakamura: J. Phys. Chem. Solids **62** (2001) 389.
9) Y. Takano, K. Hiraki, H. M. Yamamoto, T. Nakamura, and T. Takahashi: J. Phys. Chem. Solids **62** (2001) 393.
10) Y. Takano, K. Hiraki, H. M. Yamamoto, T. Nakamura, and T. Takahashi: Syn. Met. **120** (2001) 1081.
11) S. Iwai, K. Yamamoto, F. Hiramatsu, H. Nakaya, Y. Kawakami,

and K. Yakushi: Phys. Rev. B **77** (2008) 125131.

12) H. Mori, S. Tanaka, and T. Mori: Phys. Rev. B **57** (1998) 12023.

13) M. Watanabe, Y. Noda, Y. Nogami, and H. Mori: J. Phys. Soc. Jpn. **73** (2004) 116.

14) K. Bender, K. Dietz, H. Endres, H. W. Helberg, I. Hennig, H. J. Keller, H. W. Schafer, and D. Schweitzer: Mol. Cryst. Liq. Cryst. **107** (1984) 45.

15) T. Kakiuchi, Y. Wakabayashi, H. Sawa, T. Takahashi, and T. Nakamura: J. Phys. Soc. Jpn. **76** (2007) 113702.

16) K. Yamamoto, K. Yakushi, K. Miyagawa, K. Kanoda, and A. Kawamoto: Phys. Rev. B **65** (2002) 085110.

17) R. Wojciechowski, K. Yamamoto, K. Yakushi, M. Inokuchi, and A. Kawamoto: Phys. Rev. B **67** (2003) 224105.

18) H. Seo: J. Phys. Soc. Jpn. **69** (2000) 805.

19) R. H. McKenzie, J. Merino, J. B. Marston, and O. P. Sushkov: Phys. Rev. B **64** (2001) 085109.

20) R. T. Clay, S. Mazumdar, and D. K. Campbell: J. Phys. Soc. Jpn. **71** (2002) 1816.

21) T. Mori: J. Phys. Soc. Jpn. **72** (2003) 1469.

22) J. Merino, H. Seo, and M. Ogata: Phys. Rev. B **71** (2005) 125111.

23) M. Kaneko and M. Ogata: J. Phys. Soc. Jpn. **75** (2006) 014710.

24) H. Watanabe and M. Ogata: J. Phys. Soc. Jpn. **75** (2006) 063702.

25) K. Kuroki: J. Phys. Soc. Jpn. **75** (2006) 114716.

26) C. Hotta and N. Furukawa: Phys. Rev. B **74** (2006) 193107.

27) C. Hotta, N. Furukawa, A. Nakagawa, and K. Kubo: J. Phys. Soc. Jpn. **75** (2006) 123704.

28) H. Seo, K. Tsutsui, M. Ogata, and J. Merino: J. Phys. Soc. Jpn. **75** (2006) 114707.

29) M. Udagawa and Y. Motome: Phys. Rev. Lett. **98** (2007) 206405.

30) Y. Tanaka and K. Yonemitsu: J. Phys. Soc. Jpn. **76** (2007) 053708.

31) S. Miyashita and K. Yonemitsu: Phys. Rev. B **75** (2007) 245112.

32) Y. Tanaka and K. Yonemitsu: J. Phys. Soc. Jpn. **77** (2008) 034708.

33) Y. Tanaka and K. Yonemitsu: J. Phys. Soc. Jpn. **78** (2009) 018002.

34) S. Miyashita and K. Yonemitsu: J. Phys. Soc. Jpn. **77** (2008) 094712.

35) S. Nishimoto, M. Shingai, and Y. Ohta: Phys. Rev. B **78** (2008) 035113.

36) B. Rothaemel, L. Forró, J. R. Cooper, J. S. Schilling, M. Weger, P. Bele, H. Brunner, D. Schweitzer, and H. J. Keller: Phys. Rev. B **34** (1986) 704.

37) For α-I$_3$, we use the symbol A′ in stead of D which is used in ref. 32.

38) A. Kobayashi, S. Katayama, K. Noguchi, and Y. Suzumura: J. Phys. Soc. Jpn. **73** (2004) 3135.

39) A. Kobayashi, S. Katayama, and Y. Suzumura: J. Phys. Soc. Jpn. **74** (2005) 2897.

40) S. Katayama, A. Kobayashi, and Y. Suzumura: J. Phys. Soc. Jpn. **75** (2006) 054705.

41) A. Kobayashi, S. Katayama, Y. Suzumura, and H. Fukuyama: J. Phys. Soc. Jpn. **76** (2007) 034711.

42) N. Miyashita, M. Kuwabara, and K. Yonemitsu: J. Phys. Soc. Jpn. **72** (2003) 2282.

43) S. Miyashita, Y. Tanaka, S. Iwai, and K. Yonemitsu: submitted to J. Phys. Soc. Jpn.

44) K. Yamamoto, S. Iwai, S. Boyko, A. Kashiwazaki, F. Hiramatsu, C. Okabe, N. Nishi, and K. Yakushi: J. Phys. Soc. Jpn. **77** (2008) 074709.